Thixoforming of A356/SiC and A356/TiB_2 Nanocomposites Fabricated by a Combination of Green Compact Nanoparticle Incorporation and Ultrasonic Treatment of the Melted Compact

SINAN KANDEMIR, HELEN V. ATKINSON, DAVID P. WESTON, and SARAH V. HAINSWORTH

Thixoforming is a type of semi-solid processing which is based on forming metals in the semi-solid state rather than fully liquid or solid state. There have been no reports of the thixoforming of nanocomposites in the literature. The incorporation of ceramic nanoparticles into liquid metals is a challenging task for the fabrication of metal matrix nanocomposites due to their large surface-to-volume ratio and poor wettability. Previous research work by a number of workers has highlighted the challenges with the incorporation of nanoparticles into liquid aluminum alloy. In the present study, SiC and TiB_2 nanoparticles with an average diameter between 20 and 30 nm were firstly incorporated into green compacts by a powder forming route, and then the compacts were melted and treated ultrasonically. The microstructural studies reveal that the engulfment and relatively effective distribution of the nanoparticles into the melt were achieved. The hardness was considerably improved with only 0.8 wt pct addition of the nanoparticles. The nanocomposites were successfully thixoformed at a solid fraction between 0.65 and 0.70. The microstructures, hardness, and tensile mechanical properties of the thixoformed nanocomposites were investigated and compared with those of the as-received A356 and thixoformed A356 alloys. The tensile properties of the thixoformed nanocomposites were significantly enhanced compared to thixoformed A356 alloy without reinforcement, indicating the strengthening effects of the nanoparticles.

DOI: 10.1007/s11661-014-2501-0

I. INTRODUCTION

METAL matrix nanocomposites (MMNCs) strengthened with nano-sized ceramic or other hard particles have shown their potential to significantly improve mechanical properties of light alloys such as those based on aluminum beyond the properties of conventional metal matrix composites (where the reinforcement particles are micron-sized).[1–5] While the ductility of the matrices deteriorates with the addition of micron-sized ceramic particles due to their tendency to crack during mechanical loading and relatively high reinforcement concentration in the matrix,[6] it could be maintained or even improved with a low addition of nanoparticles, *e.g.*, 0.5 or 1.0 wt pct.[5,7] These enhancements in the mechanical properties by nanoparticles are associated with the obstruction of dislocation movement and also the promotion of fine grain sizes.[8–10] Also, it is crucial to achieve a uniform distribution of nanoparticles through the matrix and good bonding between the matrix and nanoparticles in order to maximize composite mechanical properties.[11–13]

Although there are a number of available fabrication routes for MMNCs, an ultrasonic method,[5,14] which combines casting with ultrasonic cavitation-based dispersion of nanoparticles in molten alloys, seems an economical and promising route in terms of producing engineering components with complex shapes.[7,15] In the fabrication of MMNCs by liquid state routes, poor wettability (which can affect the bonding at the reinforcement-matrix interface) and the tendency of ceramic nanoparticles to agglomerate and cluster due to their large surface-to-volume ratio are the main barriers to obtaining a uniform dispersion of nanoparticles into the matrix.[5] However, it has been shown that good dispersion of ceramic nanoparticles in molten metals is possible with the ultrasonic method due to high intensity ultrasonic waves with localized implosive impact, namely transient cavitation, and acoustic streaming.[15–17] It has been assumed that ultrasonic cavitation could break up nanoparticle clusters due to the collapse of cavitation bubbles when they reach a critical size in the clusters.[18] Acoustic streaming which is a circulating flow is then considered to play a role for distributing nanoparticles throughout the matrix.

In addition to the barriers mentioned, the incorporation of nanoparticles into the melt, *i.e.*, a nanoparticle feeding mechanism, is a most critical consideration in the fabrication of nanocomposites by ultrasonic melt

SINAN KANDEMIR, Lecturer, is with the Department of Mechanical Engineering, Izmir Institute of Technology, Izmir, Turkey. Contact e-mail: sinankandemir@iyte.edu.tr HELEN V. ATKINSON and SARAH V. HAINSWORTH, Professors, and DAVID P. WESTON, Lecturer, are with the Department of Engineering, University of Leicester, Leicester, UK.

Manuscript submitted April 1, 2014.
Article published online August 14, 2014

treatment for effective particle distribution,[19] as nanoparticles should be fed slowly just under the ultrasonic probe where the maximum ultrasonic intensity occurs.[20–22] Several nanoparticle feeding mechanisms including a manual nanoparticle feeding from the top of the melt,[16] crucible placement approach,[23] double capsulate feeding,[15] and flux-assisted feeding[19] have been investigated to achieve particle entry into the melt. However, the majority of these nanoparticle feeding mechanisms have not been found to be promising in terms of incorporation of nanoparticles into the melt, mainly due to the formation of oxide on the liquid aluminum surface and oxide formation on aluminum foil in the case of the double capsulate feeding.[24,25] In this work, a mechanism which is based on mixing the nanoparticles with pure aluminum powders and pressing them together to make small tablets has been employed prior to treatment of molten alloy with ultrasonics. This particular mechanism involving powder metallurgy is called the 'green compact' method. With this method, the aim is for all nanoparticles to be completely embedded in solid and then held in the melt before they are distributed by ultrasonic cavitation. Also, it is envisioned that the nanoparticles will be gradually released from the tablets being wetted by molten aluminum as the aluminum powders melt.

Thixoforming is one type of semi-solid metal processing. This involves forming metallic alloys and composites using the thixotropic behavior of materials with non-dendritic microstructure in the semi-solid state. The methods give near-net shape components and hence potentially save manufacturing cost. Thixoforming, which involves reheating a solid slug to the semi-solid state and forming it with a liquid fraction between 30 and 50 pct, offers improved mechanical properties over conventional casting, because the semi-solid metal flow is laminar rather than turbulent, hence reducing porosity. Also, thixoforming allows components to be produced with more complex shapes and lower energy demand compared to forging (reviewed in[26–28]). A majority of thixoforming studies in the literature have concentrated on conventional casting alloys, such as A356 and A357. There is a demand to widen the range of materials, including MMNCs. Although thixoforming of conventional metal matrix composites has been reported by several investigators,[29–31] it has not been tested for MMNCs yet.

Semi-solid forming of MMNCs fabricated with ultrasonic mixing was patented in the USA in 2009 by Turng *et al.*[32] This forming process relies on rheocasting which is another type of semi-solid metal processing and involves direct injection of a cooling liquid metal in the semi-solid state into a die. De Cicco *et al.*[33] utilized the same process for semi-solid AC43A zinc alloy with 0.5 wt pct SiC nanoparticle addition and showed that reduced shrinkage, progressive mold filling, and increased ductility were achieved in comparison with liquid cast monolithic AC43A and liquid cast AC43A/SiC nanocomposite. There are few available studies in the literature regarding semi-solid processing of MMNCs.

Thixoforming is feasible only when the starting material has a spheroidal microstructure. Ultrasonic processing of liquid metals is one of the routes for obtaining spheroidal microstructure.[27] The aim in this study is to thixoform ultrasonically processed MMNCs and to test the mechanical properties. The major challenges are ensuring that the nanoparticles are wetted and dispersed reasonably evenly. The method described here will involve firstly incorporating the nanoparticles with aluminum powders in green compacts and melting the compact with additional alloy and ultrasonically treating.

II. MATERIALS AND EXPERIMENTAL PROCEDURE

A. *Selection of Matrix and Reinforcement Materials*

A356 commercial aluminum casting alloy (composition shown in Table I) is widely used for thixoforming and hence was used for the fabrication of nanocomposites in this work. The main reason to select A356 alloy as the matrix material is that it contains around 7 wt pct (~6.76 at pct) silicon, which could suppress the potential chemical reaction between liquid aluminum and the SiC nanoparticles used, and prevent the formation of Al_4C_3 (brittle compound) at the particle–matrix interface below 973 K (700 °C).[34] Moreover, A356 has a relatively low melting point with ~892 K (619 °C) compared to that of pure aluminum (~933 K, 660 °C), and it is therefore expected that working with relatively low temperatures decreases the risk of attack between liquid alloy and the ultrasonic probe tip which is generally made of titanium.

Commercially available β-SiC and TiB_2 nanoparticles supplied by Nanostructured & Amorphous Materials, Inc. were used for strengthening A356 alloy. Their properties are given in Table II. SiC, which is a popular reinforcement type for aluminum composites due to its nearly identical density to that of aluminum alloys, was first selected. Second, TiB_2 which is known to be strongly wetted by aluminum compared to SiC was preferred to overcome the potential poor wettability that can be encountered for Al/SiC composites.[35]

B. *Preparation of Tablets Containing Nanoparticles*

Aluminum powders with an average particle size of 60 μm and purity of 99.8 pct were mixed with, in a first trial, 14 wt pct of SiC and in a second trial, 16 wt pct of TiB_2 nanoparticles, by simply blending them by hand in a lab jar for 5 minutes. The mixture of the powder particles and reinforcement nanoparticles was hot pressed at 600 MPa, in vacuum of 4×10^{-2} bar and at temperature of 573 K (300 °C) for 10 minutes into tablets 20 mm in diameter. The height of the tablets ranged between 4.5 and 5.5 mm depending on the amount of mixture that was placed in the press mold. When tablets with this weight percent of SiC or TiB_2 are further processed to form nanocomposites

Table I. Composition of A356 Alloy (Weight Percent)

Al	Si	Mg	Cu	Zn	Mn	Fe	Ti
Bal.	7	0.40	0.20	0.10	0.10	0.10	0.15

Table II. Nanoparticles Used for Experiments

Particle	Average size (nm)	Density (g cm^{-3})	Purity (pct)
SiC	20 to 30	3.22	>97
TiB_2	20 to 30	4.52	80 to 90

(Section II–C), the resulting target weight percent is 0.8 wt pct to roughly mimic the levels used in Yang *et al.*[5]

C. *Fabrication of Nanocomposites*

The schematic experimental arrangement including a glove box, a commercially available ultrasonic unit (Misonix sonicator S-4000 manufactured by Qsonica, LLC), and a 2 kW induction heating system (EasyHeat-Ambrell, Cheltenham Induction Heating Ltd.) is illustrated in Figure 1. The glove box was designed and produced in-house to prevent the nanoparticles escaping into the air. The ultrasonic unit for providing the vibration required to disperse the nanoparticles into the melt consists of three major components: generator, piezo-electric unit (transducer), and probe, and is capable of generating a 20 kHz ultrasonic wave with a maximum power of 600 W. The probe transmitting ultrasonic energy into the melt is made of the titanium alloy Ti-6Al-4V which is known to be a most suitable sonotrode material as it can withstand relatively high temperatures in the region of 873 K (600 °C). However, the probe supplied by the manufacturer was based upon a half wave design for operations at room temperature. At high temperatures, *e.g.*, 923 K (650 °C), when the probe heats up, the Young's modulus of the probe material, and hence the wavelength, decreases according to Eqs. [1] and [2].

$$c = \sqrt{\frac{E}{\rho}} \qquad [1]$$

where c is the velocity of sound, E is the modulus of elasticity, and ρ is the density.

$$\lambda = c/f \qquad [2]$$

where λ is the wavelength, and f is the frequency.

The shortened wavelength prevents the probe from proper tuning (generating intermittent sonication rather than the required continuous sonication). In order to solve this issue, the length of the probe can be shortened to match the shortened wavelength. However, shortening the probe may potentially damage the piezo-electric unit [which cannot withstand temperatures much above 323 K (50 °C)] due to the decreased distance to the heat source (liquid alloy and the probe tip). Instead, a solid mass of another half wavelength made from Ti-6Al-4V alloy 117-mm long and 12.7-mm diameter was attached to the ultrasonic probe for producing a full wave ultrasonic probe shifting the piezo-electric unit further away from the heat source.

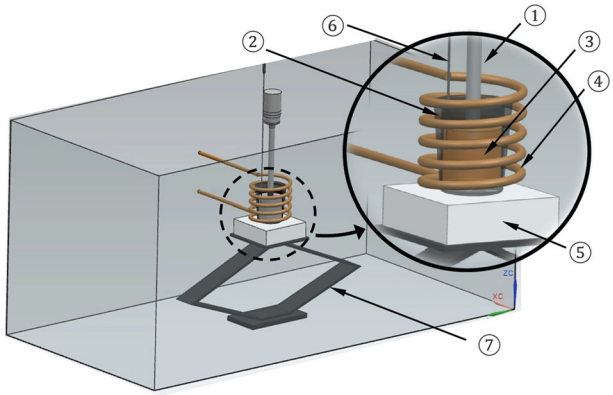

Fig. 1—Schematic of experimental setup for ultrasonic treatment of alloys in the glove box; 1: Ultrasonic probe, 2: Crucible, 3: Liquid alloy, 4: Induction coil, 5: Ceramic block, 6: K-type thermocouple, 7: Screw jack.

Approximately, 60 g of A356 alloy chunks was charged into a graphite crucible with an average diameter of 38- and 52-mm height, and melted with induction heating and held at ~973 K (700 °C) for 15 minutes for homogenization. A green compact tablet was placed onto the melt surface, and the ultrasonic probe was then dipped about 13 mm into the melt pushing the tablet under the surface of the melt from where it was floating, as illustrated in Figure 2. The temperature was decreased to 943 K (670 °C), and sonication was applied with the titanium probe at 70 to 80 W for 30 minutes at this temperature ensuring that the tablet was completely melted. After the ultrasonic process, the probe was removed from the melt, and the liquid composite was left to solidify in the crucible in ambient conditions to room temperature. The total amount of the nanoparticles (SiC and TiB_2) in a composite was calculated to be 0.8 wt pct.

D. *Thixoforming*

A schematic illustration of the thixoforming press is shown in Figure 3. The details of the thixoforming press acting vertically upwards have been described previously.[36,37] Billets 25 mm in diameter and 25 mm in length, whose volume corresponds to that of the die cavity, were machined from fabricated A356/SiC and A356/TiB_2 nanocomposites. The nanocomposite billets were induction heated to 848 K (575 °C) corresponding to ~30 pct liquid fraction in three steps to 773 K, 833 K, and 848 K (500 °C, 560 °C, and 575 °C) in 9 minutes holding the temperature of the billet at each step,

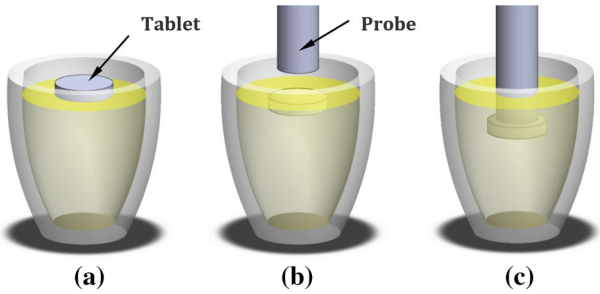

Fig. 2—Schematic of green compact nanoparticle incorporation mechanism; (*a*) positioning of a tablet on the melt surface, (*b*) submerging the ultrasonic probe into the A356 melt, and (*c*) ultrasonic processing of the tablet which is pushed down by the probe into the melt.

2 minutes at 773 K (500 °C), 1 minute at 833 K and 848 K (560 °C and 575 °C) as appropriate multi-step induction heating minimizes the temperature gradient of the billet. The heating process was established using two K-type thermocouples (0.5 mm sheath diameter), positioned at a depth of 10 mm from the top of the billet, one in the center and the other 5 mm from the outer surface. In actual tests, only one thermocouple, one near the outer surface of the billet was used, for ease of operation. Once the desired temperature was reached, and the thermocouple was extracted, the billet was thixoformed into the die. The die was made of EN24T tool steel and was heated by cartridge heaters to 573 K (300 °C) to improve the flow of the semi-solid material into the cavity and avoid premature freezing. The ram velocity was 70 mm/s throughout the stroke. The resulting complete thixoformed sample is shown in Figure 4. In addition to the nanocomposites, the unreinforced A356 alloy was ultrasonically treated for 30 minutes and then thixoformed under the same experimental conditions for comparison. Hence, any difference in the properties of these two samples (thixoformed A356 and thixoformed nanocomposites) is most likely to be due to the nanoparticles and not other aspects.

E. *Microstructural Characterization*

The samples were ground and polished to a 0.25 μm finish using a diamond-based suspension. Microstructural analyses were performed with an Olympus BX51 optical microscope and an FEI Sirion 200 field emission gun scanning electron microscope (FEGSEM) fitted with a Princeton Gamma Technology Avalon energy dispersive X-ray spectroscopy (EDX) system to determine phase composition. In order to ascertain whether or not the nanoparticles were embedded into the matrix and any chemical reaction occurred at the matrix-particle interface, the dispersion of nanoparticles in the tablets and fabricated nanocomposites was also investigated by means of a JEOL 2100 transmission electron microscope (TEM) equipped with an EDX system (Princeton Gamma Technology Avalon), operating at an accelerating voltage of 200 kV. Selected area electron diffraction (SAED) measurements were performed with this TEM. The nanocomposite TEM samples were in the form of a 3-mm disk which was punched from the nanocomposite sheets 100 to 120 μm thickness. These

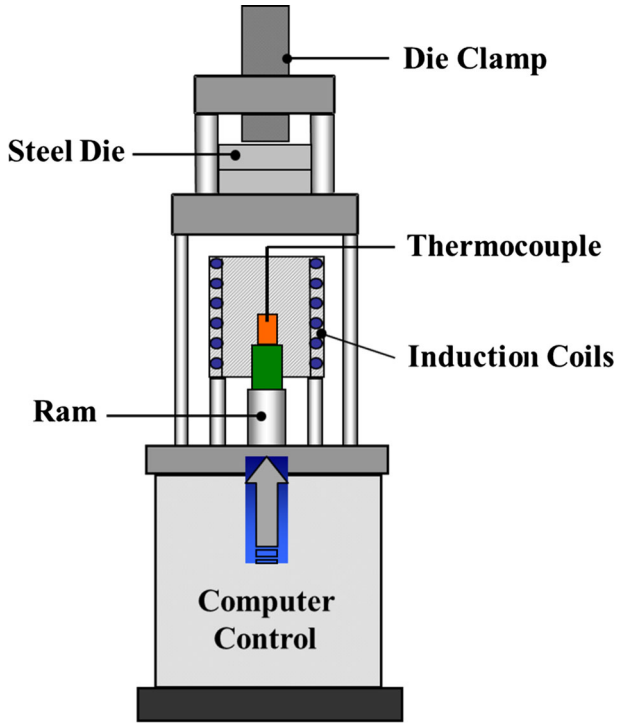

Fig. 3—Schematic of the thixoforming press.

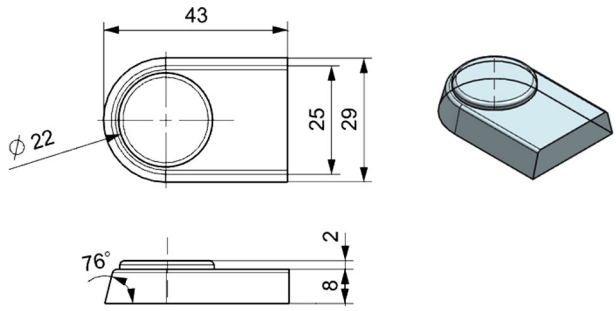

Fig. 4—Dimensions of the resulting thixoformed sample (in mm).

were obtained by grinding a 2-mm slice with 600 grit SiC paper. Each disk was ground and polished to about 50- to 70-μm thickness with a 1000 grit SiC paper, followed by dimpling at the center using a Gatan 656 Mk3 dimple grinder. For the final polishing to perforation, thus obtaining electron transparent areas, the dimpled disks were ion-milled with a Gatan precision ion beam polishing system under an argon atmosphere. The ion milling parameters were 4° angle, 4 kV gun voltage, and 3 rpm disk rotation. In addition, a Metris X-TEK XT H 225 model X-ray CT machine with an operating voltage of 225 kV was used to observe any interior feature or defects in the thixoformed nanocomposites.

F. *Mechanical Testing*

Vickers hardness tests were carried out using a Mitutoyo MV-1S macrohardness tester under the conditions of 5 kgf load, 10 seconds load time, and 50 μm/s

loading speed for the cast and thixoformed samples. Each hardness value is the average of at least 25 measurements. Specimens for tensile testing were machined from the A356 ingot, the thixoformed A356 alloy, and the thixoformed nanocomposites according to ASTM E 8/E 8M-08 standards. Appropriate tensile specimens could not be produced from the nanocomposite casts due to the limited dimension of the crucible, and hence the tensile properties of the nanocomposite casts were not investigated. The specimens were dog bone style tensile bars with a gage length of 16 mm and a gage section diameter of 4 mm. The tensile tests were performed using a 3345-model Instron tensile testing machine with 2 mm/min crosshead speed at room temperature. A 10 mm extensometer was used to obtain accurate force–displacement data, and four tensile specimens were tested for each sample.

III. RESULTS AND DISCUSSION

A. *Microstructural Characterization of the Tablets*

The microstructures of the SiC and TiB_2 tablets are given in Figures 5 and 6, respectively. The nanoparticles tend to be clustered in the as-supplied state and, when mixed with the aluminum powders, the clusters tend to be preserved. The images indicate that the nanoparticle clusters were distributed through the microstructure and are in the interstices between the aluminum grains which have been deformed by the pressing. Simple mixing and compaction did not break up the microclusters. Figure 7 shows the EDX analysis, in which Si and C maps correspond to the SiC nanoparticles, for a selected area in the microstructure of the SiC nanocomposite tablet. Also, the EDX mapping of an area for the tablet containing TiB_2 nanoparticles is presented in Figure 8. The Ti map illustrates where the TiB_2 nanoparticle clusters were located. In order to further examine the degree of contact between the nanoparticles and aluminum in the compact, TEM studies were conducted for the SiC and TiB_2 tablets as shown in Figures 9 and 10, respectively. It is clear from both figures that the compaction of the aluminum powders and nanoparticles has induced relatively effective embedding of nanoparticles in the aluminum at the interface, as indicated in Figures 9(b) and 10(b) with arrows.

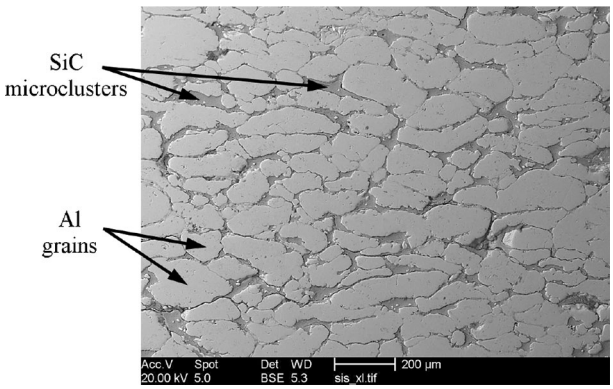

Fig. 5—Backscattered electron (BSE) image of the green compact containing 14 wt pct SiC nanoparticles.

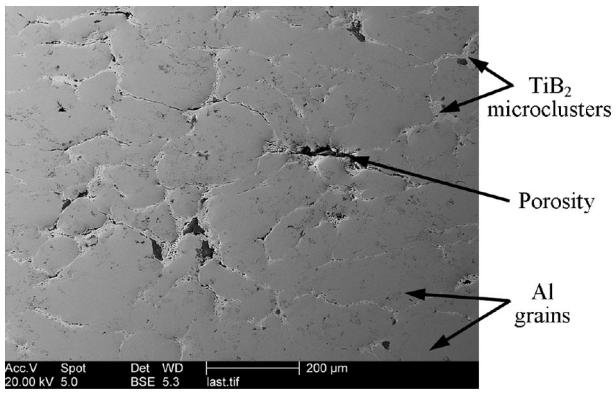

Fig. 6—BSE image of the green compact containing 16 wt pct TiB_2 nanoparticles.

B. *Microstructural Characterization of the Fabricated Nanocomposites*

Figure 11 compares the optical micrographs of the pure A356 alloy, ultrasonically processed A356 alloy for 30 minutes at 943 K (670 °C) without the addition of nanoparticles, and the fabricated nanocomposites (A356/0.8 wt pct SiC and A356/0.8 wt pct TiB_2). It can be seen from Figure 11(b) that ultrasonic treatment of the alloy without nanoparticles has noticeably refined the microstructure changing the morphology of α-aluminum grains from large dendrites to a relatively fine and globular structure with eutectic located in interglobular regions compared to the pure alloy (Figure 11(a)). However, the ultrasonically treated alloy

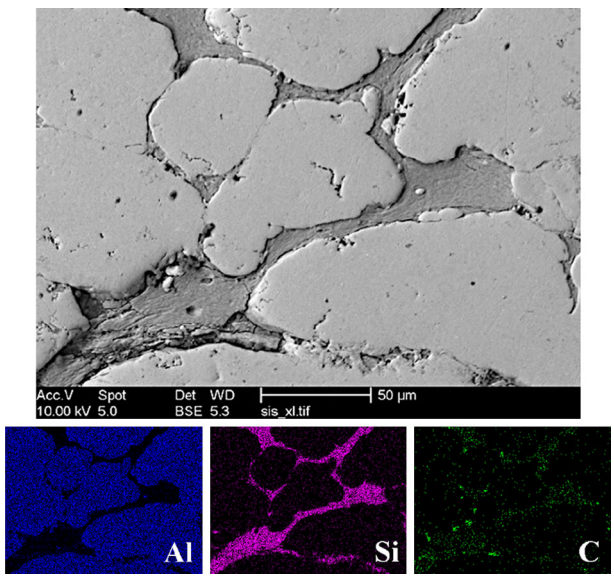

Fig. 7—BSE image and EDX mapping of a selected area in the SiC nanoparticle green compact showing the aluminum grains and the clusters of the nanoparticles.

still displays some dendrites as marked with the dashed lines in the microstructure. Figures 11(c) and (d) show the typical microstructures of the A356/0.8 wt pct SiC and A356/0.8 wt pct TiB_2 nanocomposites, respectively. In comparison to the ultrasonically processed A356 alloy, large dendrites were further broken, and α-aluminum grains were refined upon the addition of nanoparticles. Comparing Figures 11(c) and (d), there is little difference between the effects of SiC and TiB_2. The microstructure of a slice cut from a typical nanocomposite (A356/SiC) was investigated in order to document any microstructural changes created in different locations of the cast, as shown in Figure 12. The region which corresponds to the location of the probe during the processing, *i.e.*, the high cavitation zone, showed relatively large pores (image 1 in Figure 12). This severe

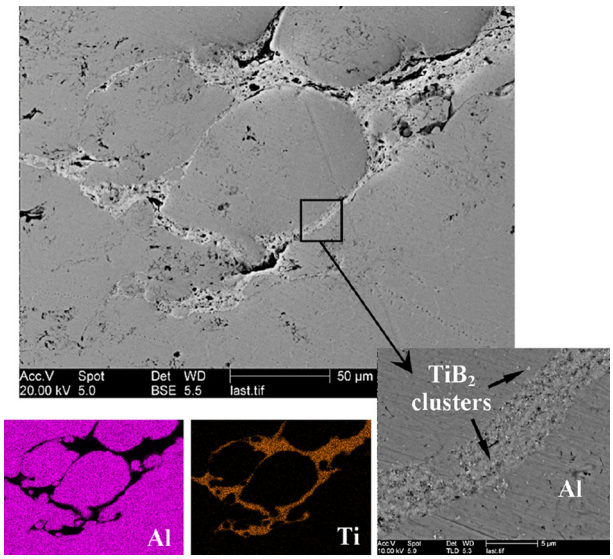

Fig. 8—BSE image and EDX mapping of a selected area in the TiB_2 nanoparticle green compact showing the aluminum grains and the clusters of the nanoparticles.

porosity formation could be ascribed to the acoustic streaming as the violent flow created by ultrasonic vibration could trap argon or any gas bubbles from the melt surface into the melt, leading to microcavities in the cast after solidification.[18]

A typical FEGSEM image of the A356/0.8 wt pct SiC nanocomposite at low magnification is presented in Figure 13(a). In addition to grain refinement due to the ultrasonic treatment and nanoparticle addition, some large and blocky particles which could be Al_3Ti due to the chemical reaction between the Ti probe and liquid aluminum, along with porosity, were observed in the microstructure of the composite. The EDX spot analysis performed on this particle implies that the particle is most likely to be Al_3Ti given the atomic percentage ratios if the presence of silicon originating from the matrix is ignored, as shown in Figure 13(b). It is expected that Al_3Ti can form at 938 K (665 °C).[38] The melt is at 943 K (670 °C) explaining why the reaction has occurred.

Figure 14 indicates the location of some SiC nanoparticles although the particle size means the particles are hard to locate in the FEGSEM. It is thought that some nanoparticle clusters which are around or less than 1 μm in size remain in the microstructure. It can be observed from the EDX mapping in Figure 14 that the nanoparticles were embedded inside the aluminum grain indicating that they could act as a nucleation site due to their potential to act as nucleants.[10] With conventional metal matrix composites, the micron-size reinforcements tend to be pushed to the grain boundaries (the eutectic) by the solidification front, which may lead to deterioration in the mechanical properties.[39] It was not possible to identify the individual nanoparticles with the EDX analysis due to the spatial resolution limit of the system. However, it was possible to perform EDX spot analyses on some clusters of nanoparticles. For example, Figure 15(b) illustrates the EDX analysis carried out for the cluster shown in Figure 15(a). In order to determine the degree of nanoparticle distribution through

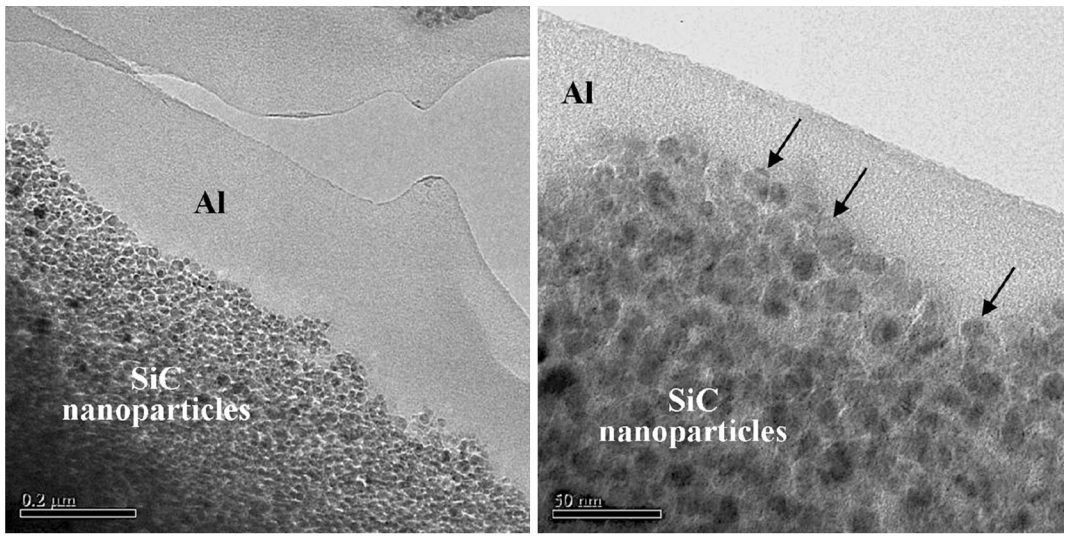

(a) (b)

Fig. 9—TEM images of the microstructure of the SiC nanoparticle compact showing the contact between the nanoparticles and aluminum.

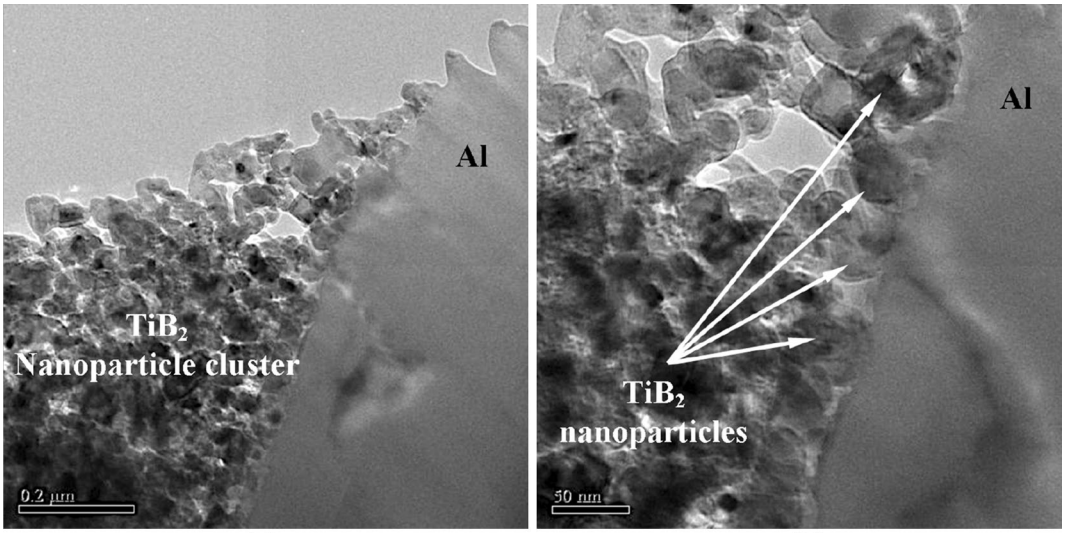

Fig. 10—TEM microstructure of the compact containing TiB_2 nanoparticles (Image b was taken at high magnification).

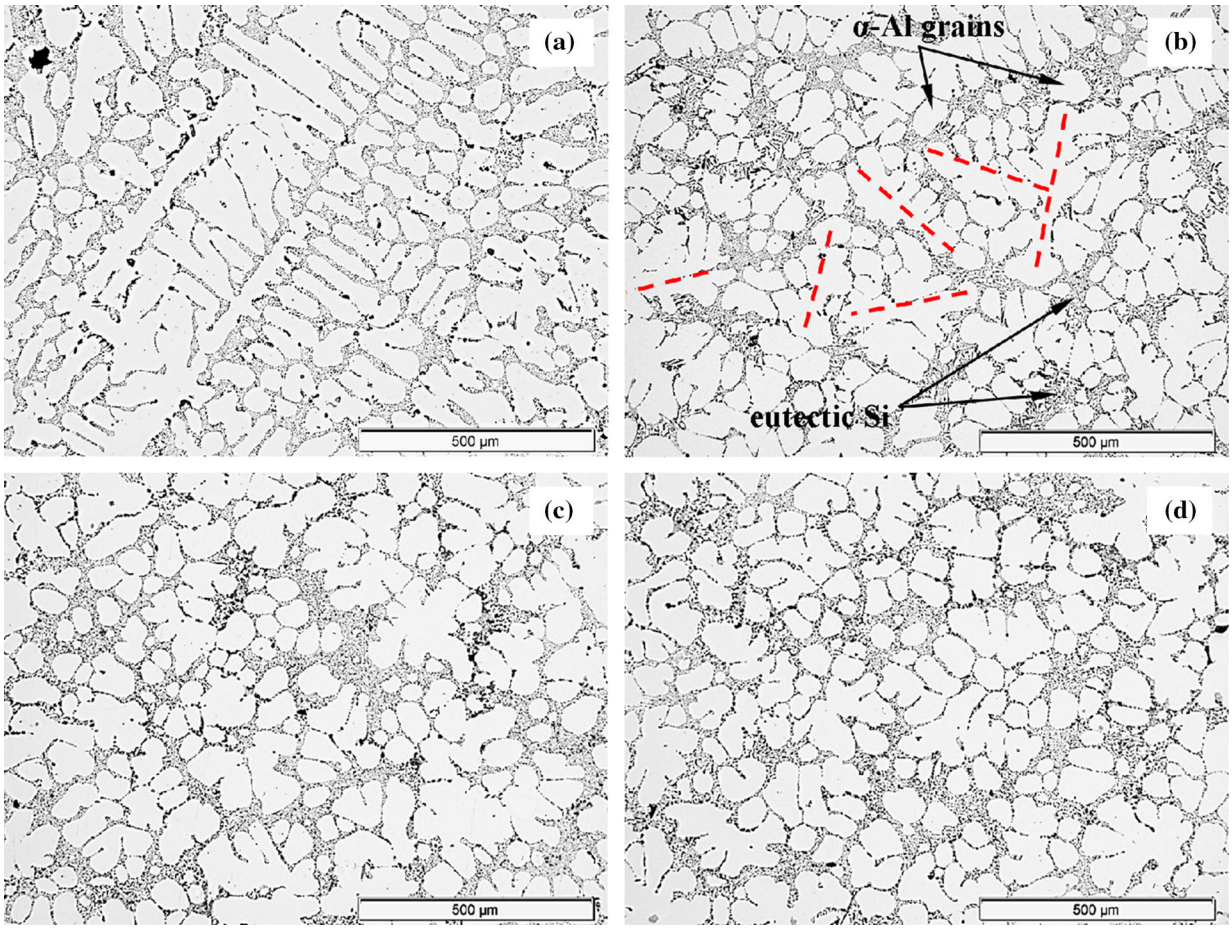

Fig. 11—Comparison of the optical micrographs of (*a*) pure A356 alloy, (*b*) 30 min ultrasonically treated A356 alloy at 943 K (670 °C) without reinforcement, (*c*) A356/0.8 wt pct SiC, and (*d*) A356/0.8 wt pct TiB_2 nanocomposites produced with 30 min sonication.

the matrix, the microstructure of a slice cut which could document the distribution of nanoparticles by ultrasonic method for the whole cast, was investigated. Figure 16 represents the distribution of the SiC nanoparticles for several locations through the composite slice. Some micron-size clusters of nanoparticles were found (*e.g.*,

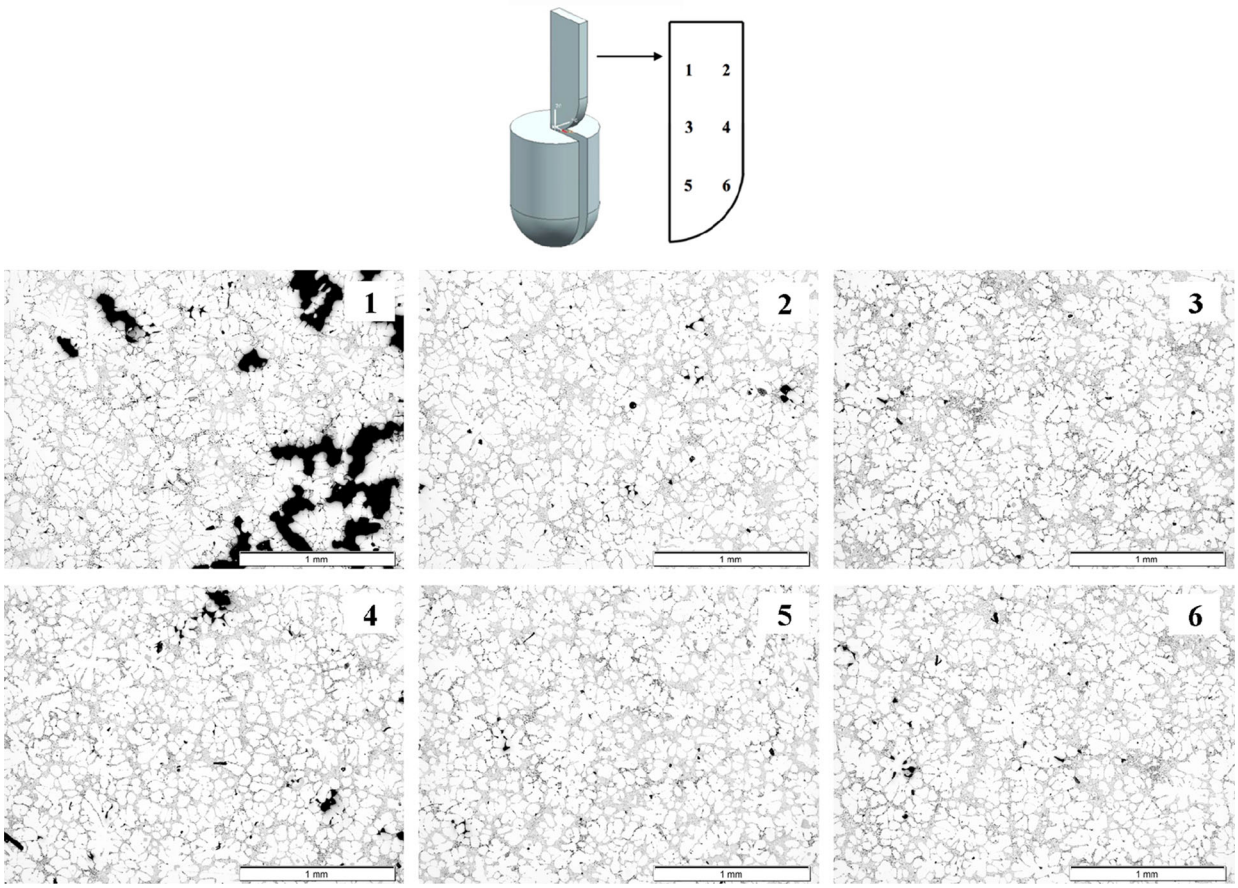

Fig. 12—Optical micrographs of different locations through a cast slice of A356/0.8 wt pct SiC nanocomposite.

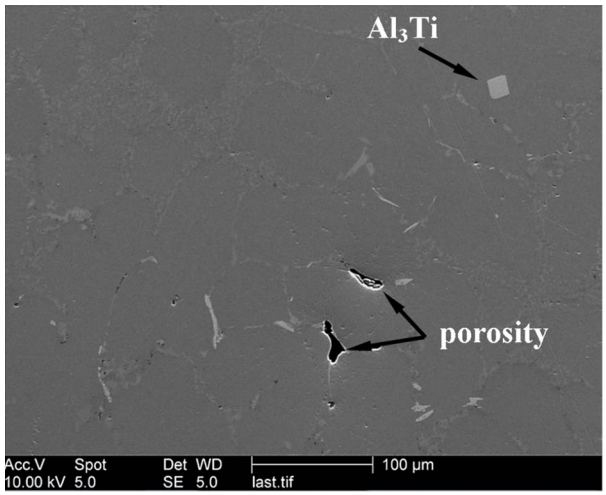

(a)

	Al	Si	Ti	V
wt.%	50.1	11.1	38.2	0.6
at.%	60.7	12.9	26.0	0.4

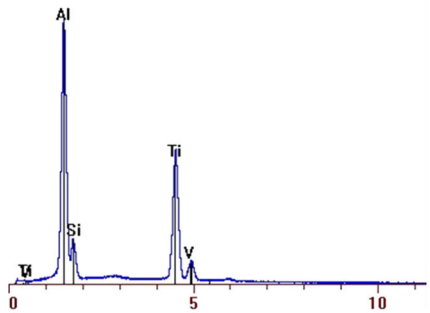

(b)

Fig. 13—(*a*) Secondary electron (SE) image of the A356/0.8wt.SiC nanocomposite, and (*b*) EDX analysis of the relatively large and blocky particle (Al_3Ti) in a.

Figures 16(4) and (6)). Images 6-1 and 6-2 in Figure 16 present some of these clusters which may be due to particle absorption by gas bubbles. However, the cluster in image 6-2 is more likely to be a remnant piece of the compact, which has not been completely dispersed. Once the compacts were introduced into the melt, they sank and tended to attach to the crucible wall around the region of 6. In this area, the intensity of ultrasonic cavitation is relatively low. The oxide layers shown in image 6-2, which could have been formed during the preparation of

compact, were also likely to act as barriers to the dispersion of nanoparticles. It is also observed that remnant compact pieces were pushed to the eutectic region like micron-sized reinforcements (*e.g.,* image 6 in Figure 16).

A356/0.8 wt pct TiB_2 nanocomposite also displayed nanoparticles almost everywhere in the microstructure (Figure 17). Possible undispersed pieces of the compact containing TiB_2 were also found in the cast near the crucible wall as illustrated in Figure 18 with the EDX analysis. One interesting observation between the A356/SiC and A356/TiB_2 nanocomposites is that while the SiC nanoparticles were often found as clusters which are nano or sub-micron size in the microstructure (Figure 14), the TiB_2 nanoparticles generally appear as individual particles or ultrafine clusters (consisting of a couple of nanoparticles) in the matrix (Figure 17(b)). This difference in the settling of the nanoparticles in the cast could be attributed to the enhanced wettability of TiB_2 by aluminum in comparison to SiC.

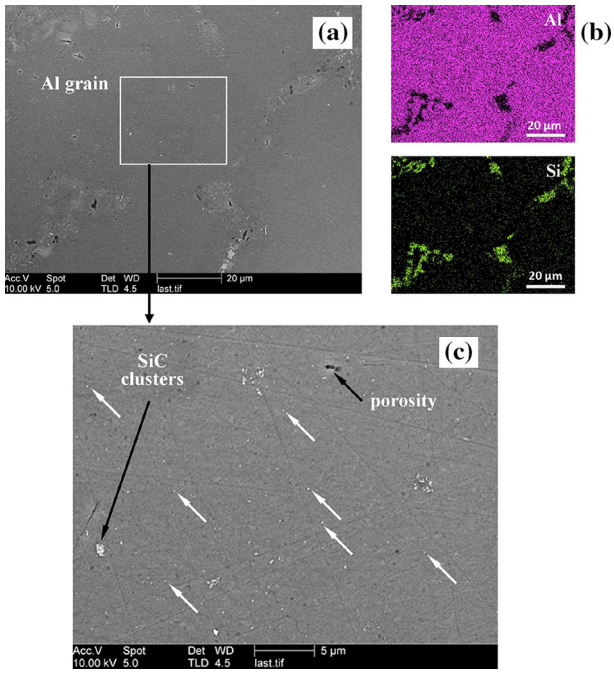

Fig. 14—(*a*) SE image from the A356/SiC nanocomposite, (*b*) Al and Si EDX mapping for the whole microstructure in a, and (*c*) SE image of the area shown with a white square in a indicating the dispersion of the SiC nanoparticles and their clusters in the matrix (Some individual nanoparticles are marked with white arrows).

The presence and dispersion of nanoparticles through the matrix was also investigated with TEM imaging and SAED in order to ascertain whether or not the nanoparticles were embedded into the matrix and whether any chemical reaction had occurred between the matrix alloy and reinforcement. Figure 19 shows a TEM image of the composite. As seen in the figure, the SiC particles were usually present as nanoclusters in the microstructure, which coincides with the FEGSEM investigations. One of these nanoclusters was magnified in Figure 20(a) for EDX analysis. The EDX analysis in Figure 20(b) shows a silicon peak which potentially indicates the presence of SiC nanoparticles in the aluminum matrix. It should be noted that the EDX system available here was not suitable for identifying carbon incontrovertibly. Oxygen in the analysis is more likely to be arisen from the oxidation of the SiC particles during the compaction process or TEM specimen preparation. Figure 20(d) represents the indexed SAED pattern of the area centring the dashed circle shown in Figure 20(a), and this pattern consists of the rings for the nanoparticles which are single crystalline SiC with fcc cubic structure. There is no an observed transition layer between the matrix and the particles at nano level, hence demonstrating that no chemical reaction has taken place, as

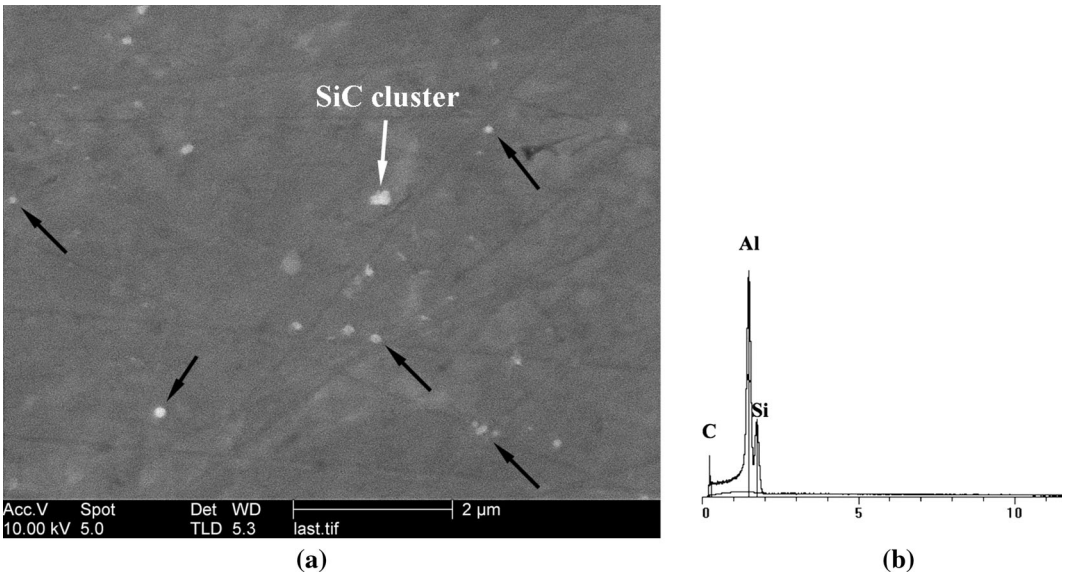

Fig. 15—(*a*) SE image showing the dispersion of the SiC nanoparticles with a cluster at high magnification (Some individual nanoparticles are marked with black arrows), and (*b*) EDX analysis of the cluster shown in a.

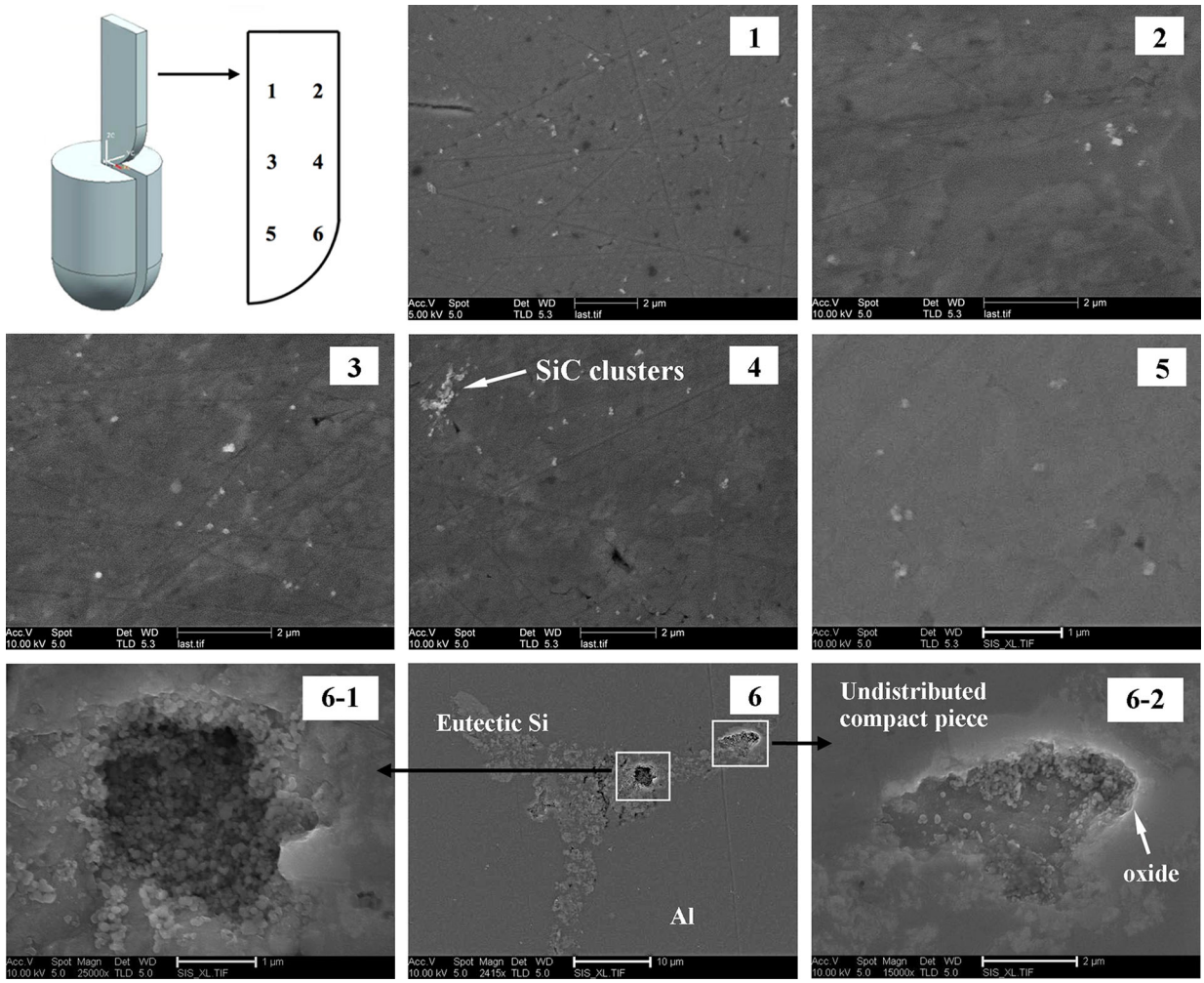

Fig. 16—High magnification SE images of A356/0.8 wt pct SiC nanocomposite revealing the distribution of the SiC nanoparticles throughout the composite slice.

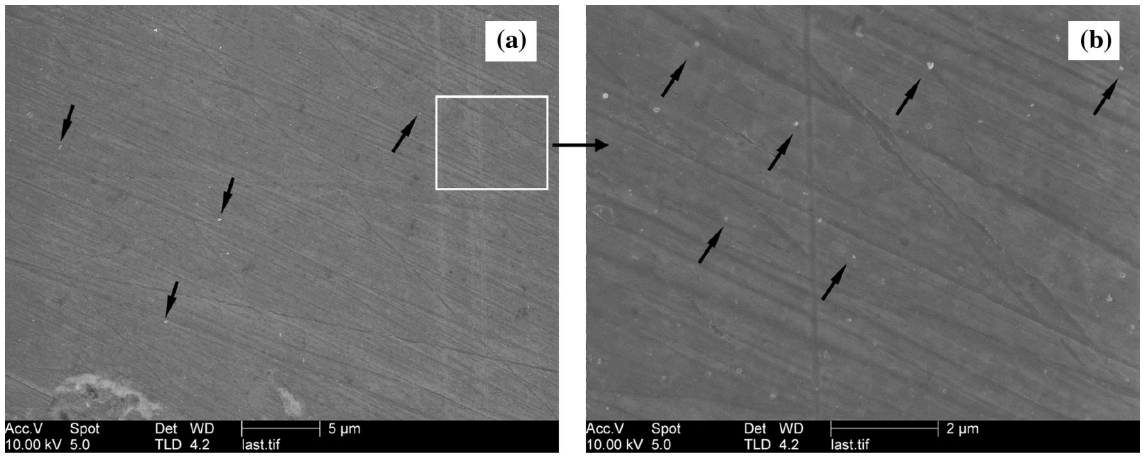

Fig. 17—SE image of the A356/0.8wt pct TiB_2 nanocomposite indicating some possible individual TiB_2 nanoparticles or ultrafine clusters with black arrows.

shown in Figure 20(e) (consistent with Reference 40). The TEM image of the composite containing TiB_2 nanoparticles with the EDX analysis is given in Figure 21(a). The SAED pattern and EDX analysis in Figure 21 both confirmed the presence of TiB_2 and that the particles were embedded into the matrix. Also,

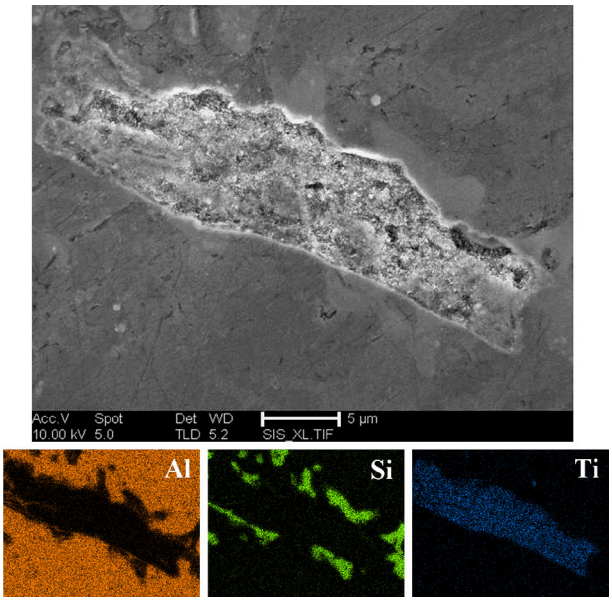

Fig. 18—SE image of a remnant piece of the TiB_2 compact in the matrix with the EDX mapping.

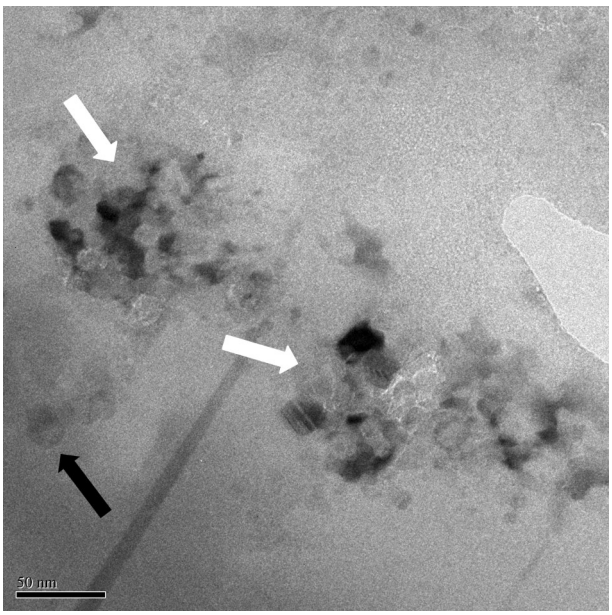

Fig. 19—TEM image of the A356/0.8wt pct SiC nanocomposites indicating an embedded individual nanoparticle with the black arrow and particle clusters with the white arrows.

Figure 21(e) may imply that a clear bonding was achieved between the TiB_2 nanoparticles and aluminum. The nanoparticles have been found as both clusters and individual particles in the matrix, consistent with the observations in the FEGSEM.

C. *Thixoforming of the Nanocomposites*

Thixoforming of the aluminum nanocomposites produced with the combination of the green compact nanoparticle incorporation method followed by ultrasonic melt treatment resulted in successful filling of the cavity. However, radiography of a thixoformed component *e.g.*, as shown in Figure 22, exhibits porosity and cracks concentrated near the end of material flow. The detailed microstructure of a typical thixoformed nanocomposites part, namely A356/SiC nanocomposite, through the longitudinal section is shown in Figure 23. Forming the nanocomposite billet in the semi-solid state has significantly reduced the porosity in comparison with the nanocomposite cast after the fabrication process, especially around the location of the probe (Figure 12). When the alloy is in the semi-solid state, the 'liquid' phase which is likely to be the lower melting point eutectic in A356 alloy spreads between the globules, and promotes displacements of the grains.[41] In the final stages of solidification, shrinkage porosity and cracks may form in the interglobular regions.[42] This suggests that the cracks and porosity at the end of flow shown in the radiograph of the thixoformed part in Figure 22 could be due to the lack of liquid phase at that region. Apart from the end of thixoformed part, the decrease in the porosity for the whole nanocomposite could be explained with the high solid fraction in thixoforming, 70 pct, and the relatively good feeding of A356 alloy due to the presence of silicon in the alloy.

One of the main observations is the morphology of the grains in the microstructure of the thixoformed components. Images a, b, d, e, f, and n in Figure 23 show generally globular structure compared to the as-cast nanocomposite (Figure 12) due to the partial remelting of the eutectic region surrounding the grains. If the thixoforming temperature and holding time in the semi-solid state are increased, the globules are expected to be rounder. Images c, i, k, l, m, and o in Figure 23 show elongated grains. This is thought to be associated with the design of the die and/or a relatively high solid fraction in the semi-solid billet. Although the corner of the die and cavity is rounded, the concentration of the elongated grains was not prevented at those regions. It should be highlighted that the effective solid fraction may not be 70 pct due to the fact that induction heating in the present work may have led to a temperature gradient through the semi-solid billet. McLelland *et al.*[36] pointed out that the presence of SiC particles in conventional metal matrix composites increases the effective solid fraction, and hence the viscosity. However, the very small proportion of the nanoparticles with 0.8 wt pct in the present work is unlikely to affect the viscosity significantly.

Figure 24 shows the FEGSEM images of the thixoformed A356/SiC and A356/TiB_2 nanocomposites in areas free from highly elongated grains (*e.g.*, e in Figure 23).

D. *Hardness Testing*

Vickers hardness tests have been conducted on the following specimens: pure A356 alloy, 30 minutes ultrasonically treated A356 alloy, A356/0.8wt pct SiC, and A356/0.8wt pct TiB_2 cast nanocomposites, and the thixoformed nanocomposites. The average hardness results for all specimens are presented in Figure 25, with error bars obtained from the standard deviation of

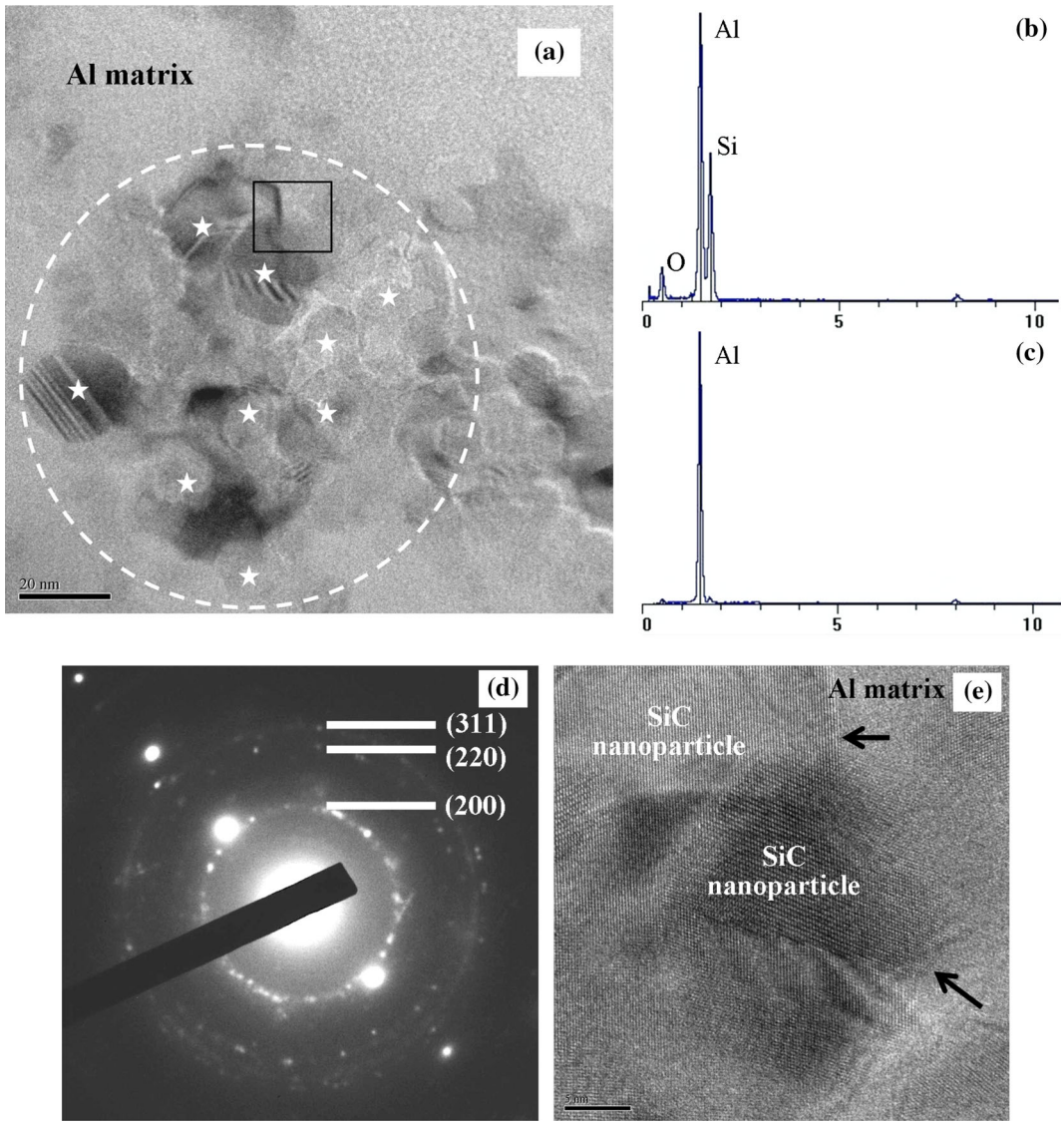

Fig. 20—(*a*) TEM image of the A356/0.8 wt pct SiC nanocomposite indicating some SiC nanoparticles with the stars, (*b*) EDX spectrum of the area shown with a dashed circle in a, (*c*) EDX spectrum of the matrix, (*d*) SAED pattern of the SiC particles in a indexed for SiC, and (*e*) high magnification TEM image of the bonding between the matrix and the SiC particles marked with a black square in a.

at least 25 indentations for each sample. Ultrasonic treatment of A356 did not alter the hardness, but the standard deviation has reduced significantly, indicating that the sonication has made the grain structure more homogenous. These results are also consistent with the work of Yu *et al.*[43].

0.8 wt pct addition of both SiC and TiB_2 nanoparticles has enhanced the hardness of the alloy by about 6 pct; the results for SiC and TiB_2 are very similar. The increment in the hardness may be due to the grain refining effect of nanoparticles and/or Orowan strengthening where the nanoparticles act as barriers to the dislocation motion. However, the ultrasonic treatment without the addition of nanoparticles refined the dendritic microstructure of A356 alloy, but this did not improve the hardness. This indicates that for the nanocomposites, it is mainly Orowan strengthening leading to the improvement in hardness.

It should be noted that porosity content can affect the hardness, leading to fluctuations in the measurements through the sample. In some regions, where higher hardness values are measured, this may reflect the fact that an effective distribution of nanoparticles has been achieved. However, the regions showing relatively lower hardness values may contain significant pores leading to lower hardness even though they may have dispersed nanoparticles. The relatively large indent (the average diagonal length is ~0.360 to 0.370 mm) in the present study, means that it is usually not possible to perform the measurement on regions completely free from pores, and therefore, the hardness may not fairly reflect the effect of the nanoparticle distribution on hardness.

Thixoforming of the nanocomposite casts at 848 K (575 °C) further enhanced the hardness as it significantly reduced the porosity. It is observed that the hardness of the thixoformed A356/TiB_2 composite is higher than

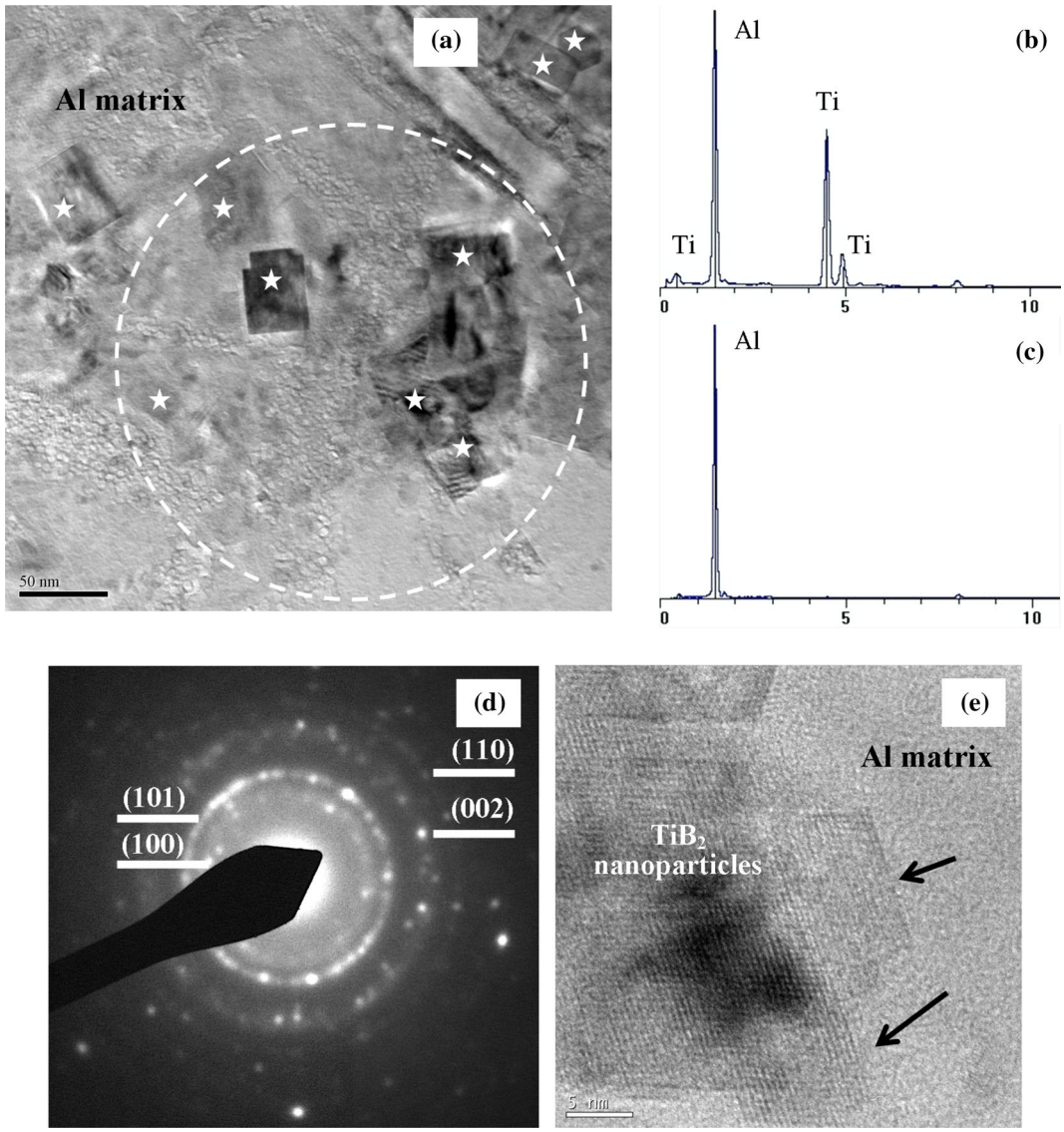

Fig. 21—(*a*) TEM image of the A356/0.8 wt pct TiB_2 composite indicating some TiB_2 nanoparticles with the stars, (*b*) EDX spectrum of the area shown with a dashed circle in a, (*c*) EDX spectrum of the matrix, (*d*) SAED pattern of the TiB_2 particles in a indexed for TiB_2, and (*e*) high magnification TEM image of the bonding between the matrix and the TiB_2 particles.

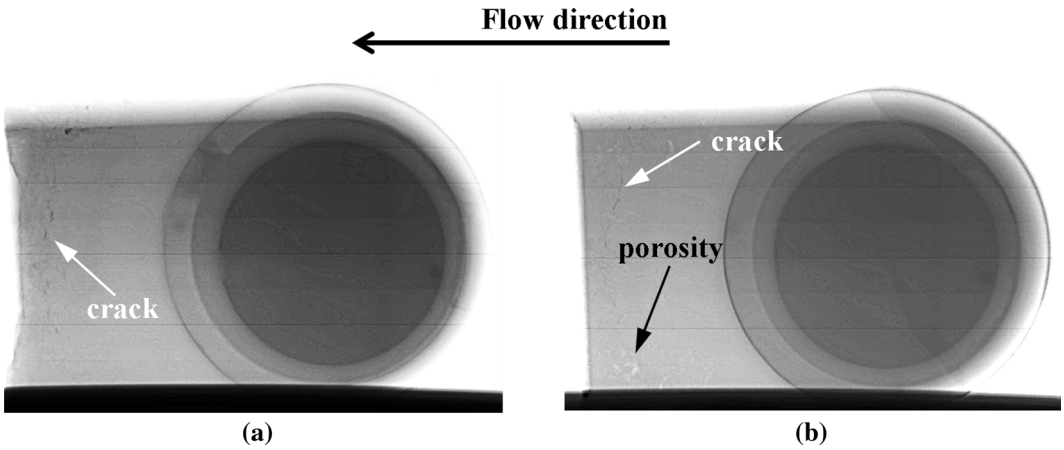

Fig. 22—Radiographs of the thixoformed nanocomposites: (*a*) A356/SiC and (*b*) A356/TiB_2 at 848 K (575 °C) with 70 mm/s ram velocity.

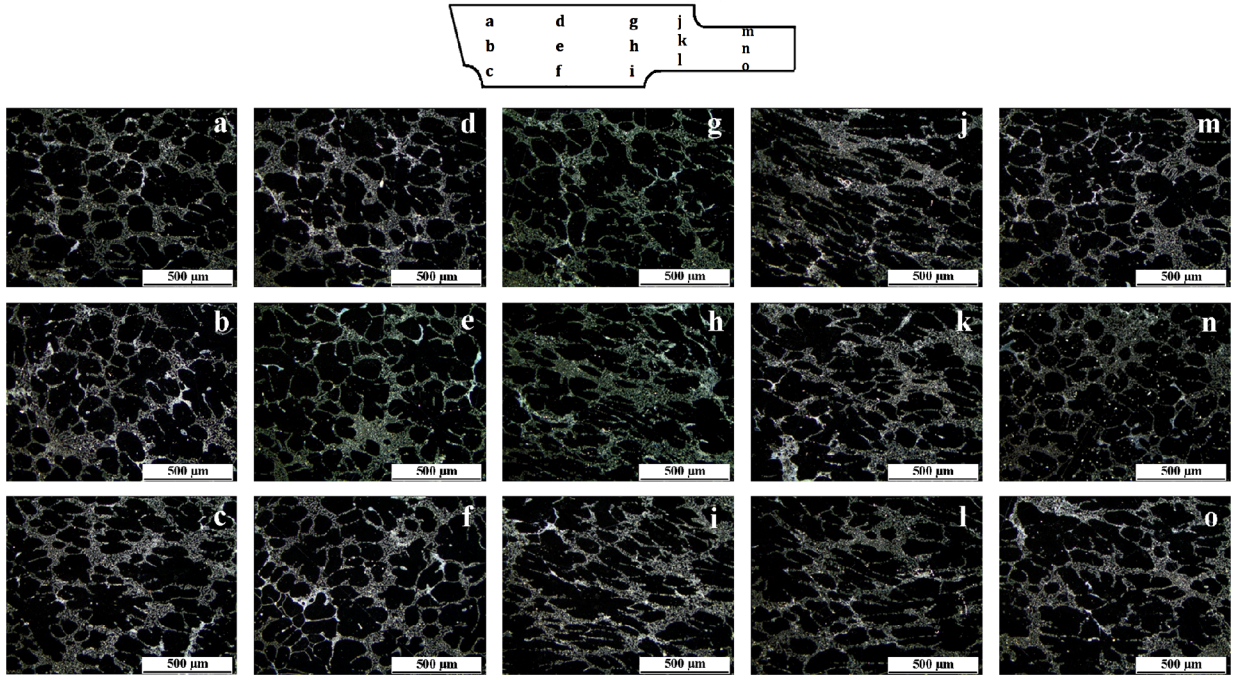

Fig. 23—Dark-field optical images of the longitudinal section through a thixoformed nanocomposite (A356/0.8wt pct SiC).

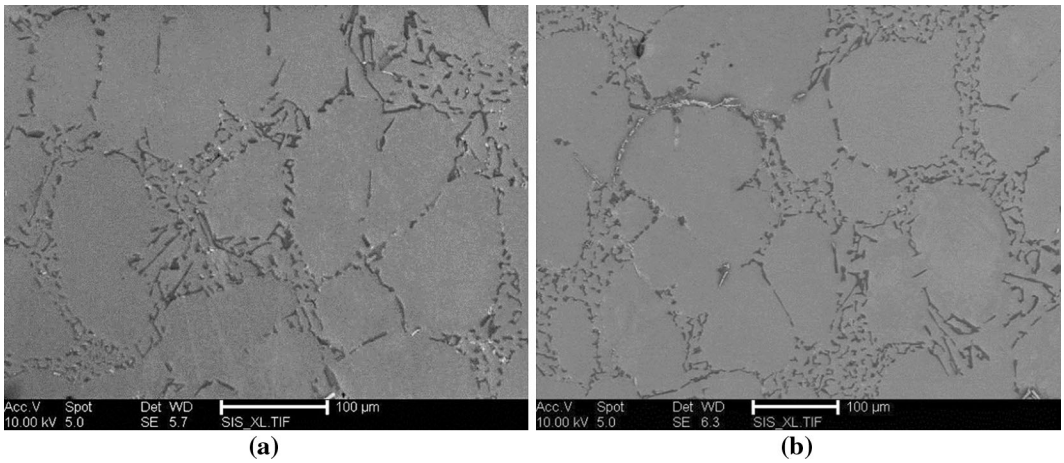

Fig. 24—SE images of thixoformed (*a*) A356/0.8 wt pct SiC, and (*b*) A356/0.8 wt pct TiB_2 nanocomposites (area e in Fig. 23).

that of the thixoformed A356/SiC composite. The difference could be explained with better distribution of TiB_2 nanoparticles into the matrix compared to the SiC nanoparticles, which was confirmed with the FEG-SEM and TEM analyses. However, other effects such as porosity, Al_3Ti or variation in microstructure through the thixoformed sample may be coming into play.

E. *Tensile Testing*

The 0.2 pct proof stress, ultimate tensile strength (UTS), and elongation to fracture data are presented in Table III for A356 alloy, ultrasonically treated and thixoformed A356 alloy, thixoformed A356/SiC, and A356/TiB_2 nanocomposite specimens.

The 0.2 pct proof stress and UTS of the ultrasonically treated and thixoformed A356 alloy were improved in comparison with that of the cast alloy. Although there is scatter in the results, the average elongation to fracture of the thixoformed alloy also tends to increase. It is likely that these improvements are due to the fact that semi-solid processing refined the microstructure and reduced the porosity. Regarding the nanocomposites, while A356/SiC showed similar average 0.2 pct proof strength with 108 ± 6 MPa to that of thixoformed alloy (110 ± 11 MPa), the composite containing TiB_2 nanoparticles displayed improved 0.2 pct proof strength in comparison. Also, the average UTS was improved for both the thixoformed A356/SiC and A356/TiB_2 nanocomposites. The strength enhancement of nanocomposites is likely

to be associated with Orowan strengthening with the nanoparticles (as discussed for hardness earlier). In conventional metal matrix composites with micron-sized reinforcement, particle load bearing and enhanced dislocation density due to coefficient of thermal expansion mismatch mechanisms play a significant role. Here relatively low nanoparticle concentration in the matrix, *i.e.*, 0.8 wt pct, means that these mechanisms cannot operate. The TiB_2 nanoparticles give greater strength enhancement compared to the SiC particles. This is likely to be related to better wetting of TiB_2 by aluminum and hence relatively uniform distribution of the TiB_2 nanoparticles. In contrast, the SiC nanoparticles tend still to be present as nano- or microclusters in the microstructure.

The average elongation to fracture values of the thixoformed A356/SiC and A356/TiB_2 nanocomposites with 6.7 ± 2.9 and 6.9 ± 1.35 pct, respectively, is significantly higher than those of the thixoformed alloy without nanoparticles (4.6 ± 2.9 pct). In some previous work,[5,16] this was not the case, but other workers[44,45] did find same improvement. Figure 11 shows that nanoparticles enhance the formation of spheroidal eutectic (note the needle-shaped Si particles in the eutectic in Figure 11(b) *vs* the more spheroidal eutectic microstructure in Figures 11(c) and (d)). The spheroidal Si is more resistant to fracture and tends to inhibit void formation hence leading to a greater elongation to fracture.

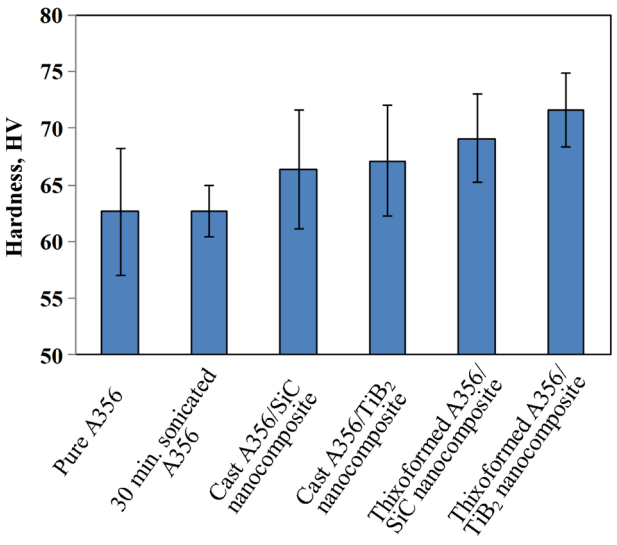

Fig. 25—Hardness of A356 alloy; 30 min. sonicated A356 alloy; cast A356/SiC and A356/TiB_2 nanocomposites; thixoformed A356/SiC and A356/TiB_2 nanocomposites.

The tensile fracture surfaces of the thixoformed alloy and thixoformed A356/SiC and A356/TiB_2 nanocomposites were analyzed with FEGSEM (Figure 26). Although all fractographs of the tensile specimens have a typical ductile fracture surface, they show some different features (Figure 26(a) porosity may have resulted in premature failure, Figure 26(b) Al_3Ti may have nucleated cracks).

The number of specimens tested here is relatively small because of the difficulty in obtaining material. The results are therefore indicative rather than definitive but do suggest further work is worthwhile.

IV. CONCLUSIONS

1. The green compact nanoparticle incorporation method which is based on the compaction of the mixture of nanoparticles and matrix powders to be added into the melt under ultrasonic cavitation, has been found to be a promising mechanism for dispersion of the nanoparticles into molten aluminum, which is the main challenge in the fabrication of MMNCs.
2. It has been shown that both the addition of 0.8 wt pct SiC and 0.8 wt pct TiB_2 nanoparticles (20 to 30 nm) into A356 alloy resulted in further grain refinement upon ultrasonic treatment of the unreinforced alloy. No distinction was observed between the grain refinement effects of these particles. They were mainly pushed into the α aluminum grains unlike micron-sized reinforcements, but the undispersed compact pieces appeared in the grain boundaries. However, while the SiC nanoparticles were often found as clusters, the TiB_2 nanoparticles generally existed as individual particles in the matrix most probably due to better wettability of TiB_2 nanoparticles in liquid aluminum.
3. The feasibility of thixoforming as a means of achieving near-net shapes in MMNCs has been demonstrated. The porosity in the A356/SiC and A356/TiB_2 nanocomposites which originated in the casting of nanocomposites was significantly reduced with thixoforming at 848 K (575 °C) (corresponding to ~30 pct liquid fraction) with a ram velocity of 70 mm/s.
4. Hardness, 0.2 pct proof stress, UTS, and elongation to fracture were generally higher (there is one exception for 0.2 pct proof stress for the samples with SiC nanoparticles) in the thixoformed nanocomposites than in the sonicated and thixoformed A356 (which in turn was higher than for cast

Table III. Tensile Properties of the A356 Alloys and their Thixoformed Nanocomposites

Specimen	0.2 pct Proof Stress (MPa)	Ultimate Tensile Strength (MPa)	Elongation to fracture (pct)
A356	77 ± 7.5	118 ± 10	2.4 ± 1.2
Sonicated and thixoformed A356	110 ± 11	159 ± 19	4.6 ± 2.9
Thixoformed A356/0.8wt pct SiC	108 ± 6	199 ± 26	6.7 ± 2.9
Thixoformed A356/0.8wt pct TiB_2	125 ± 13.5	222 ± 23	6.9 ± 1.3

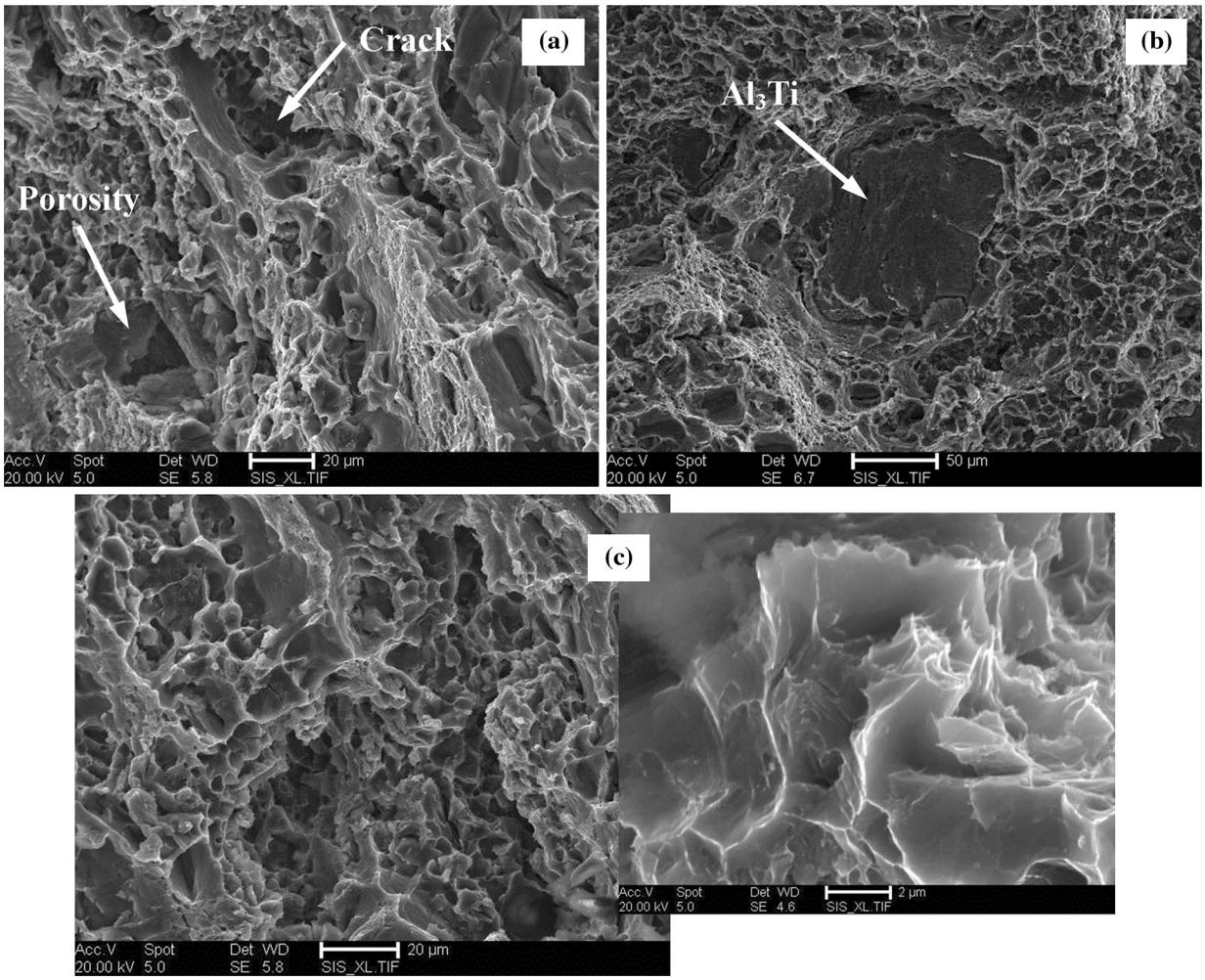

Fig. 26—Fracture surfaces of the tensile specimens from (*a*) thixoformed A356 alloy, (*b*) thixoformed A356/0.8 wt pct SiC, and (*c*) A356/0.8 wt pct TiB_2 nanocomposites.

A356). However, the number of samples is small, hence warranting further investigation.

ACKNOWLEDGMENTS

The authors would like to acknowledge the University of Leicester for the provision of laboratory facilities, and Prof Jan Dutkiewicz and Dr Lukasz Rogal at the Institute of Metallurgy and Materials Science of the Polish Academy of Sciences, Krakow, Poland, for carrying out the tablet preparation. The Turkish Ministry of National Education is also thanked for the award of a PhD scholarship to Sinan Kandemir.

REFERENCES

1. X.C. Tong and H.S. Fang: *Metall. Mater. Trans. A*, 1998, vol. 29A, pp. 893–902.
2. S.F. Hassan and M. Gupta: *Mater. Sci. Technol.*, 2004, vol. 20, pp. 1383–88.
3. S.F. Hassan and M. Gupta: *J. Compos. Mater.*, 2007, vol. 41, pp. 2533–43.
4. A. Mazahery, H. Abdizadeh, and H.R. Baharvandi: *Mater. Sci. Eng., A*, 2009, vol. 518, pp. 61–64.
5. Y. Yang, J. Lan, and X. Li: *Mater. Sci. Eng., A*, 2004, vol. 380, pp. 378–83.
6. K. Akio, O. Atsushi, K. Toshiro, and T. Hiroyuki: *J. Jpn. Inst. Light Met.*, 1999, vol. 49, pp. 149–54.
7. M. De Cicco, H. Konishi, G. Cao, H. Choi, L.S. Turng, J.H. Perepezko, S. Kou, R. Lakes, and X. Li: *Metall. Mater. Trans. A*, 2009, vol. 40A, pp. 3038–45.
8. Y. Li, Y.H. Zhao, V. Ortalan, W. Liu, Z.H. Zhang, R.G. Vogt, N.D. Browning, E.J. Lavernia, and J.M. Schoenung: *Mater. Sci. Eng., A*, 2009, vol. 527, pp. 305–16.
9. Z. Zhang and D.L. Chen: *Scr. Mater.*, 2006, vol. 54, pp. 1321–26.
10. M. De Cicco, L.S. Turng, X. Li, and J.H. Perepezko: *Metall. Mater. Trans. A*, 2011, vol. 42A, pp. 2323–30.
11. E.A. Feest: *Composites*, 1994, vol. 25, pp. 75–86.
12. A.E. Karantzalis, S. Wyatt, and A.R. Kennedy: *Mater. Sci. Eng., A*, 1997, vol. 237, pp. 200–06.
13. M.G. McKimpson and T.E. Scott: *Mater. Sci. Eng., A*, 1989, vol. 107, pp. 93–106.
14. J. Lan, Y. Yang, and X. Li: *Mater. Sci. Eng., A*, 2004, vol. 386, pp. 284–90.
15. H. Choi, M. Jones, H. Konishi, and X. Li: *Metall. Mater. Trans. A*, 2012, vol. 43A, pp. 738–46.
16. Y. Yang and X. Li: *J. Manuf. Sci. Eng. Trans. ASME*, 2007, vol. 129, pp. 252–55.

17. G. Cao, H. Konishi, and X. Li: *J. Manuf. Sci. Eng. Trans. ASME*, 2008, vol. 130, pp. 031105.1–031105.6.
18. X. Li, Y. Yang, and X. Cheng: *J. Mater. Sci.*, 2004, vol. 39, pp. 3211–12.
19. S. Kandemir, D.P. Weston, and H.V. Atkinson: *Solid State Phenom.*, 2013, vols. 192–193, pp. 66–71.
20. O. Dahlem, J. Reisse, and V. Halloin: *Chem. Eng. Sci.*, 1999, vol. 54, pp. 2829–38.
21. P.R. Gogate, P.A. Tatake, P.M. Kanthale, and A.B. Pandit: *AIChE J.*, 2002, vol. 48, pp. 1542–60.
22. A. Kumar, T. Kumaresan, A.B. Pandit, and J.B. Joshi: *Chem. Eng. Sci.*, 2006, vol. 61, pp. 7410–20.
23. S. Kandemir, A. Yalamanchili, and H.V. Atkinson: *Key Eng. Mater.*, 2012, vols. 504–506, pp. 339–44.
24. H. Choi, Y. Sun, B.P. Slater, H. Konishi, and X. Li: *Adv. Eng. Mater.*, 2012, vol. 14, pp. 291–95.
25. S. Kandemir: Ph.D. Thesis, University of Leicester, Leicester, UK, 2013.
26. D.H. Kirkwood: *Int. Mater. Rev.*, 1994, vol. 39, pp. 173–89.
27. Z. Fan: *Int. Mater. Rev.*, 2002, vol. 47, pp. 49–85.
28. H.V. Atkinson: *Prog. Mater Sci.*, 2005, vol. 50, pp. 341–412.
29. A.R.A. McLelland, H.V. Atkinson, P. Kapranos, and D.H. Kirkwood: *Mater. Lett.*, 1991, vol. 11, pp. 26–30.
30. P.J. Ward, H.V. Atkinson, P.R.G. Anderson, L.G. Elias, B. Garcia, L. Kahlen, and J.M. Rodriguez-Ibabe: *Acta Mater.*, 1996, vol. 44, pp. 1717–27.
31. M. Wenzelburger, M.N. Alsina, K. von Niessen, and R. Gadow: *Solid State Phenom.*, 2006, vols. 116–117, pp. 375–78.
32. L.S. Turng, M.P. De Cicco, and X. Li: United States Patent US 7,509,993, 2009.
33. M.P. De Cicco, X. Li, and L.S. Turng: *J. Mater. Process. Technol.*, 2009, vol. 209, pp. 5881–85.
34. J.C. Lee, J.Y. Byun, S.B. Park, and H.I. Lee: *Acta Mater.*, 1998, vol. 46, pp. 1771–80.
35. D.A. Weirauch, W.J. Krafick, G. Ackart, and P.D. Ownby: *J. Mater. Sci.*, 2005, vol. 40, pp. 2301–06.
36. A.R.A. McLelland, H.V. Atkinson, and P.R.G. Anderson: *Mater. Sci. Technol.*, 1999, vol. 15, pp. 939–45.
37. H.V. Atkinson, P. Kapranos, D. Liu, S.A. Chayong, and D.H. Kirkwood: *Mater. Sci. Forum*, 2002, vols. 396–402, pp. 131–36.
38. J. Crofton, S.E. Mohney, J.R. Williams, and T. Isaacs-Smith: *Solid-State Electron.*, 2002, vol. 46, pp. 109–113.
39. G. Wilde and J.H. Perepezko: *Mater. Sci. Eng., A*, 2000, vol. 283, pp. 25–37.
40. X. Li, Y. Yang, and D. Weiss: *Metall. Sci. Technol.*, 2008, vol. 26, pp. 12–20.
41. W. Lapkowski and M. Pietrzyk: *J. Mater. Process. Technol.*, 1994, vol. 45, pp. 365–70.
42. D. Liu: Ph.D. Thesis, University of Sheffield, Sheffield, UK, 2003.
43. S.R. Yu, H.K. Feng, Y.L. Li, and L.Y. Gong: *J. Alloys Compd.*, 2009, vol. 484, pp. 360–64.
44. M.K. Akbari, O. Mirzaee, and H.R. Baharvandi: *Mater. Des.*, 2013, vol. 46, pp. 199–205.
45. D. Wang, M.P. De Cicco, and X. Li: *Mater. Sci. Eng., A*, 2012, vol. 532, pp. 396–400.